Numerical evaluation of a novel double-concentric swirl burner for sulfur combustion

Feichi Zhang [a,*], Hosein Heidarifatasmi [a], Stefan Harth [a], Thorsten Zirwes [b,a], Robert Wang [a], Michal Fedoryk [a], Nadia Sebbar [a], Peter Habisreuther [a], Dimosthenis Trimis [a,**], Henning Bockhorn [a]

[a] Engler-Bunte-Institute, Division of Combustion Technology, Karlsruhe Institute of Technology, Engler-Bunte-Ring 1, 76131, Karlsruhe, Germany
[b] Steinbuch Centre for Computing, Karlsruhe Institute of Technology, Hermann-von-Helmholtz-Platz 1, 76344, Eggenstein-Leopoldshafen, Germany

ARTICLE INFO

ABSTRACT

A burner system for the efficient and clean combustion of sulfur is introduced, which serves as a key component in a novel solar power cycle using sulfur as chemical storage medium of solar energy. In order to validate the proposed design concept, highly-resolved numerical simulations have been performed. The current setup is operated with a thermal load of 20 kW or power density of 5 MW/m³. Two nozzle configurations with different swirl intensities (SI) of the airflow are studied. A large inner recirculation zone is observed for the nozzle with a high SI (HSI), which leads to a strong radial dispersion of the sulfur spray and a broad, short flame in the combustion chamber; although this HSI design is beneficial from the viewpoint of flame stabilization, it causes a large number of sulfur droplets hitting the chamber wall. In contrast, the nozzle design with a low SI (LSI) yields a narrow spray and a long jet flame, with much less droplets hitting the wall. The HSI nozzle shows an overall higher flame temperature compared with the LSI nozzle, which is confirmed to be caused by burning at a higher local fuel equivalence ratio. This is attributed to the strong inner recirculation flow generated by the high swirl intensity, which results in an enhanced evaporation and mixing of sulfur droplets with air. In terms of operability and NOx emission, the LSI burner is preferred due to less sulfur droplets hitting the chamber wall and the lower flame temperature.

Notation Symbols

$\dot{m}$	Mass flow rate, [kg/s]
$\dot{Q}$	Thermal load, [kW]
$\dot{q}$	Heat release rate, [W/m³]
$\dot{r}$	Chemical reaction rate, [kg/m³/s]
λ	Thermal conductivity, [W/m/K]
$\mathbf{F}$	Force, [N]
$\mathbf{g}$	Gravitational acceleration, [m/s²]
$\mathbf{j}_k$	Diffusive mass flux, [kg/m²/s]
$\mathbf{j}_q$	Heat flux, [J/m²/s]
$\mathbf{j}_j$	Diffusive flux, [kg/m²/s]
$\mathbf{u}$	Velocity vector, [m/s]
μ	Dynamic viscosity, [mPas]
ν	Kinematic viscosity, [m² /s]

ρ	Density, [kg/m³]
τ_p	Relaxation time of parcel, [s]
τ_{chem}	Chemical time scale, [s]
τ_{mix}	Mixing time scale, [s]
A_p	Surface area of the droplet, [m²]
c_p	Specific heat capacity, [J/kg/K]
D	Diffusion coefficient, [m² /s]
d	Nozzle diameter, [m]
H	Specific total enthalpy, [J/kg]
h	Heat transfer coefficient, [W/m² K]
h_{ev}	Entahlpy of evaporation, [J/kg]
Hu	Heating value, [MJ/kg]
K	Specific kinetic energy, [J/kg]
m	Mass, [kg]
N_p	Number of parcels in cell volume, [−]

* Corresponding author.
** Corresponding author.
E-mail addresses: feichi.zhang@kit.edu (F. Zhang), dimosthenis.trimis@kit.edu (D. Trimis).

p	Pressure, [Pa]
S	Source term, [$-$]
T	Temperature, [K]
V_{cell}	Cell volume, [m^3]
Y	Species mass fraction, [$-$]

Dimensionless Numbers

We	Droplet Weber number, [$-$]
Φ	Equivalence ratio, [$-$]
B_M	Spalding number, [$-$]
C_D	Drag coefficient, [$-$]
Da	Damköhler number, [$-$]
Nu	Nusselt number, [$-$]
Pr	Prandtl number, [$-$]
Re	Reynolds number, [$-$]
Sc	Schmidt number, [$-$]

Sub-/Superscripts

$\bar{\cdot}$	Spatially filtered value
$\cdot^{sgs}$	Properties evaluated at sub-grid scale
$\cdot_c$	Properties related to carrier gas
$\cdot_k$	k-th species
$\cdot_p$	Properties related to parcels
$\tilde{\cdot}$	Favre-filtered value

Acronyms

CSP	Concentrated Solar Power
HSI	High Swirl Intensity
IRZ	Inner Recirculation Zone
LES	Large Eddy Simulation
LSI	Low Swirl Intensity
PaSR	Partially Stirred Reactor
PDA	Phase Doppler Anemometry
SMD	Sauter Mean Diameter

1. Introduction

The present work is supported by the EU commission within the PEGASUS (Renewable Power Generation by Solar Particle Receiver Driven Sulfur Storage Cycle) project [1]. The overarching goal of PEGASUS is to demonstrate a novel power cycle for the utilization of solar energy. In this process, solar heat is utilized to produce elemental sulfur as chemical storage medium with a high energy density, which can be burned to generate electricity via a combined cycle power plant. The concept renders a solar power plant capable of baseload operation that enables round-the-clock renewable electricity production. As illustrated schematically in Fig. 1 on the left, sulfur is burned with air to sulfur dioxide SO_2, where the heat release from the combustion process can be used for the production of electricity. On the other hand, heat from a concentrated solar power (CSP) plant is used to decompose initial sulfuric acid (H_2SO_4) to sulfur dioxide (SO_2) and water (H_2O). The products from both sulfur-combustion and H_2SO_4-decomposition processes are then fed to the disproportionation reactor, which converts SO_2 back to H_2SO_4 and S [2]. The sulfur can be burned and the sulfuric acid can be decomposed through CSP again, leading to a closed cycle for heat or electricity production. Fig. 1 on the right shows a detailed scheme including the combined cycle for the combustion process. The heat released from the sulfur/air combustion is used to drive the gas turbine in a first stage. The product SO_2 is further oxidized catalytically to SO_3 through the "contact process", where the heat release can be used by a steam turbine to generate electricity. The product SO_3 from the "contact process" is then converted to sulfuric acid by mixing with dilute sulfuric acid in the "H_2SO_4 concentrator".

At present, studies on the combustion process of sulfur are mainly combined with the that of fossil fuels like coal, as sulfur is contained in most fossil fuels as undesired constituent [3,4]. Focus of these works is reducing the formation of sulfur oxides as pollutant emission or removal of sulfur through pyrolysis. Direct combustion of sulfur is nowadays mainly used to produce sulfuric acid, with an annual amount of over 200 Mt globally, which makes sulfuric acid a key substance in the chemical industry [5,6]. Three types of burners are generally applied for sulfur combustion [7,8].

- Rotary burner (most commonly used): the sulfur in the lower part of the horizontal rotating drum forms a molten pool as well as a thin film around the circumference of the drum. This film increases the surface area of the sulfur exposed to the incoming air and a further increase in surface area is achieved by sulfur dripping down from the top of the drum. This helps to increase the capacity of the burner and ensures that combustion is complete.
- Spray Type Burner: molten sulfur is fed to an atomizer which injects a fine spray of sulfur into the burner. At the same time the air is introduced into the combustion chamber and ignition of the sulfur takes place. The combustion chamber is fitted with baffies to mix the resultant gases and prevent any unburnt sulfur passing through to the absorption apparatus.
- Acme burner: the burner is operated with compressed air and a special sulfur melter. Sulfur is fed to the bottom of the burner via a main feed pipe, and a side feeder arm on this main feed allows for positive control of sulfur feed, thereby guaranteeing a constant level of molten sulfur in the burner.
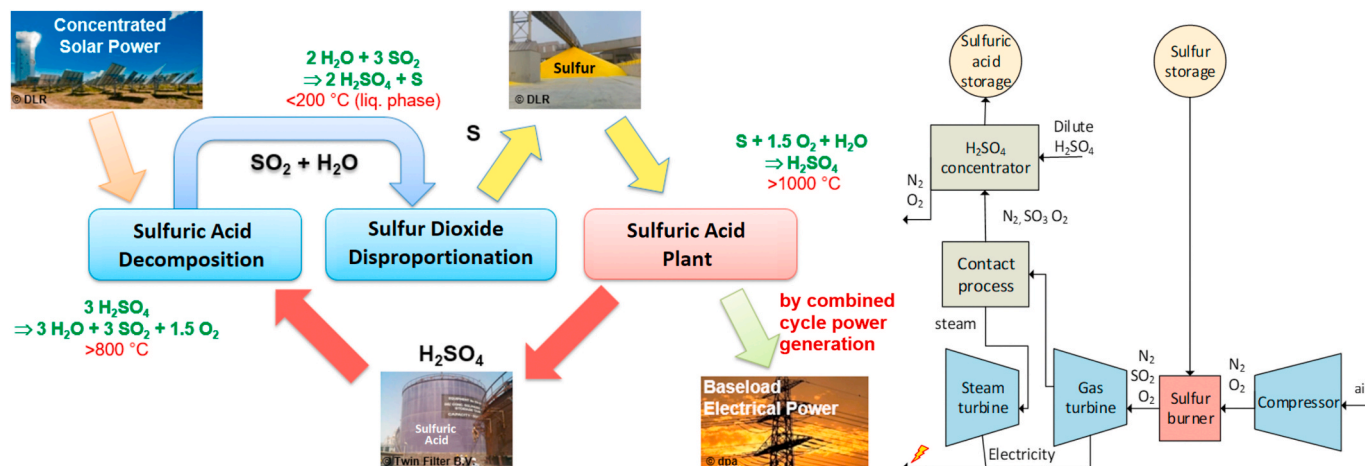

Fig. 1. Scheme of the sulfur-based thermochemical cycle for solar energy storage and utilization [1].

Steel furnaces are used for the combustion chamber, having a volume up to the order of hundreds cubic meters and lined inside with 30–50 cm of fire and insulating bricks to reduce heat losses and minimise the formation of SO_3. The residence time is typically of a few minutes [7]. As a result, most existing sulfur combustion facilities are designed for large-scale operation with a small intensity of heat release or low burning rate, respectively. Therefore, they are not suited for the combustion application in a gas turbine power plant, which is typically characterized by a short residence time and a high power density. Objective of the present work in the framework of PEGASUS is therefore to develop a novel burner system for the efficient and clean combustion of sulfur, which can be directly integrated into a gas turbine.

The application of a gas turbine operated with sulfur dioxide is favorable in terms of efficiency, as both steam and gas turbines can be used in the framework of a combined cycle gas turbine (CCGT) power plant. The burner design for sulfur combustion is however challenging in terms of suitable construction, materials and burner technology. In addition, small-scale sulfur burners with a broad load modulation range are currently not available and there is a lack of knowledge of the complex interaction of the different phenomena in the combustion process of sulfur, like turbulent flow fields, spray formation/evaporations or detailed chemical kinetics. In order to study fundamental behaviours of sulfur combustion and to assess the feasibility of coupling the sulfur burner with the overall cycle of the proposed solar power plant, a laboratory-scale burner has been designed based on available knowledge of combustor applications and technologies, e.g. for aero engines, stationary gas turbines and industrial burners. The evaluation of the performance of the burner design serves as theoretical basis for a scale-up of the burner in order to use it for real-scale gas turbines with 5 MW termal load and at an elevated pressure of up to 15 bar.

In the case of turbine combustors operated with liquid fuel, combustion processes are governed by atomization of liquid fuel and its dispersion in the combustion chamber. Under highly turbulent flow conditions the interaction between the liquid and the gaseous phase is of particular interest, as it causes spatio-temporal variations of the mixture composition and possibly undesired effects such as increased pollutant emissions due to locally high equivalence ratio. The experimental investigation of sulfur spray combustion via state-of-the-art measurement techniques, e.g. Refs. [9,10], is difficult due to limited optical access and, additionally, many relevant parameters such as the mixing or reaction rates are not assessable by means of current measurement techniques. In order to gain a more detailed insight into the spray combustion process, numerical simulations have been widely applied in the last years. Compared with simulations of solely the gas phase combustion, the most challenging task of spray combustion is given by the multiphase, multi-scale interactions between the dispersed liquid spray with both turbulent flow and combustion reaction, leading to inhomogeneities of local equivalence ratio caused by the evaporation and the mixing processes. Therefore, a large number of the numerical works conducted for spray combustion are focused on modeling the interactions between the spray, the turbulent flow and the flame [11–17]. For instance, Franzelli et al. [13] performed large eddy simulation (LES) of air/kerosene flames with both detailed and tabulated chemistry to characterize the structure and dynamics of a swirled spray flame. In Sitte et al. [14], a doubly conditional moment closure (DCMC) approach has been proposed for modeling a n-heptane/air spray flame. Filho et al. [18] studied the importance of the carrier gas thermo-chemical properties of droplets evaporating in combustion environment. Two different combustion models are analyzed in Ref. [12] for the prediction of an acetone spray flame with LES coupled with the flamelet generated manifold (FGM) method. In Ref. [11,15,16,19], LES of ethanol spray flames have been conducted using different combustion modeling concepts.

In alignment with the strategy of numerical simulations, highly-resolved LES simulation of sulfur spray combustion are conducted in this work to explore the applicability of two preliminary burner concepts with different swirler arrangements/intensities of the airflow. The simulation domain includes the major part of the nozzle. Different models have been used to consider important physical phenomena, such as the turbulent flow, spray dispersion, evaporation, mixing, ignition, flame stabilization, as well as their mutual interactions. The numerical study has been performed in a systematic way, i.e., separately for the gaseous turbulent flow and the multiphase spray combustion. Focus of the work is assessing the influence of applying different nozzle swirl intensities on the operability in terms of flame stability, burnout, collisions of sulfur droplets with walls and NOx emissions.

2. Burner design for sulfur combustion

The designed burner for sulfur combustion is given by a double-concentric swirl nozzle following the previous constructions by Kasabov et al. [20,21] and Merkle et al. [22–24], where kerosene (Jet-A1) and methane instead of sulfur have been used as fuel. Fig. 2 on the left illustrates a cross-section view of the burner system: molten sulfur is injected from a pressure swirl atomizer, which breaks up the liquid phase into a hollow-cone shaped spray downstream. A primary and a secondary swirl generator are used to create highly turbulent flows for an improved atomization and flame stabilization. The primary airflow is directed through a channel bounded by the outer periphery of the pressure atomizer and the internal wall of the prefilmer. The secondary airflow bypasses the external wall of the prefilmer and the diffusor. Both air streams meet at the lip of the prefilmer and combustion takes place further downstream the diffusor. The laboratory-scale burner is designed to work in a range of thermal loads from 10 to 50 kW, yielding a power density at ambient pressure conditions of around 5 MW/m^3 for the nominal operating point. The overall flame temperature is targeted to be in the range of 1540–1700 K depending on the operating fuel-air equivalence ratio.

The behaviour of different atomizers for generation of liquid sulfur sprays has first been analyzed with respect to required droplet sizes using empirical correlations. Airblast atomizers are able to provide the smallest droplets at high operating pressures and are preferred for this application. However, their performance is worse at ambient pressure for the laboratory scale experiments. Thus, a pressure swirl atomizer with an outer diameter of 8 mm and an injection diameter of 0.25 mm for the laboratory scale experiments is applied in this work (see the lower right part of Fig. 2), which generates a similar spray pattern at the nozzle exit compared to the airblast atomizer. The axial position of the pressure swirl nozzle can be adjusted through distance plates. The concept also allows the application of an alternative sulfur supply from the side and resignation from pressure swirl nozzle in order to operate in a pure airblast mode for future studies. Elevated air temperature is achieved in an external preheater, while the temperature of sulfur is ensured by a thermal oil cycle (indicated in Fig. 2 on the left with "Thermal conditioning").

Two arrangements of the primary and secondary swirl-generators, leading to low and high swirl intensities (LSI and HSI), have been studied in this work. The strength of the swirl is gauged by the swirl number defined as the ratio of the axial flux of angular momentum to the axial flux of the axial momentum. The switching between the HSI and LSI nozzle is accomplished by modulating the swirl intensity of the airflow for the primary and the secondary axial swirl generator, which can be replaced due to the modular structure of the burner, as shown in Fig. 3. The theoretical swirl numbers for the primary and secondary swirlers are 0.46 and 0.81 in the HSI case, and 0.76 and 0 in the LSI case. The swirler system has been designed strictly following the experimental works by Kasabov [20,21] and Merkle [22], where hydrocarbon fuels were used. In this way, a further objective for future work is to compare the burning behaviour when using sulfur instead of hydrocarbon as fuel. Finally, a cylindrical combustion chamber with dimensions of 160 mm and 200 mm in diameter and length is used for both, HSI and LSI nozzle configurations, considering a complete burnout of the sulfur spray. In
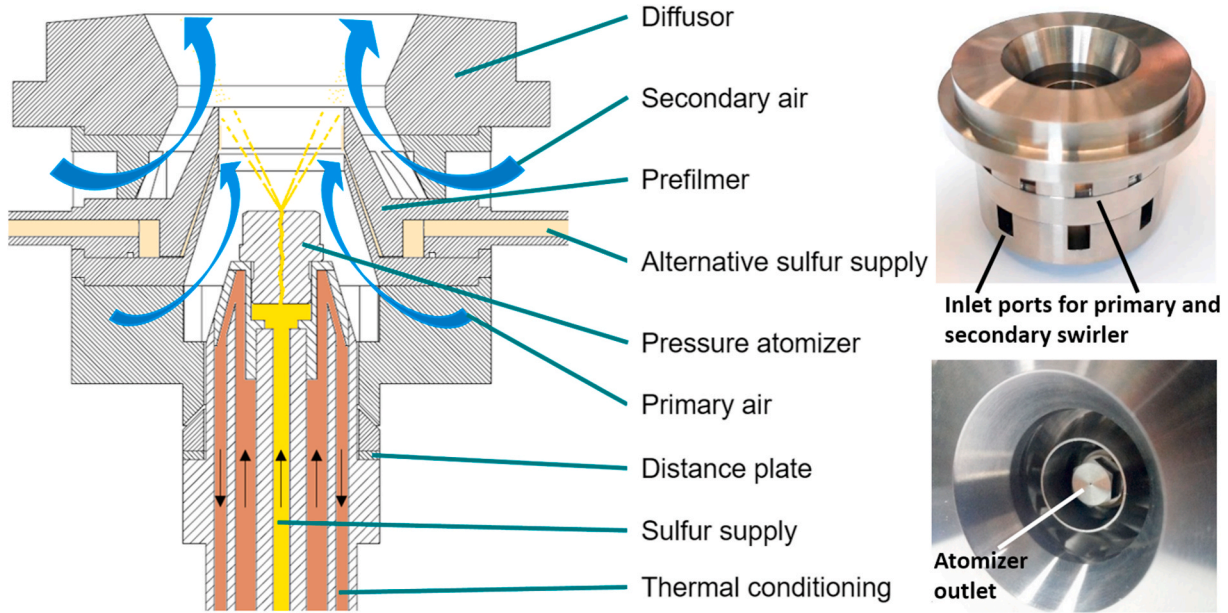
Fig. 2. Cross-section view of the developed nozzle for combustion of sulfur (left) and photos of the real nozzle (right).
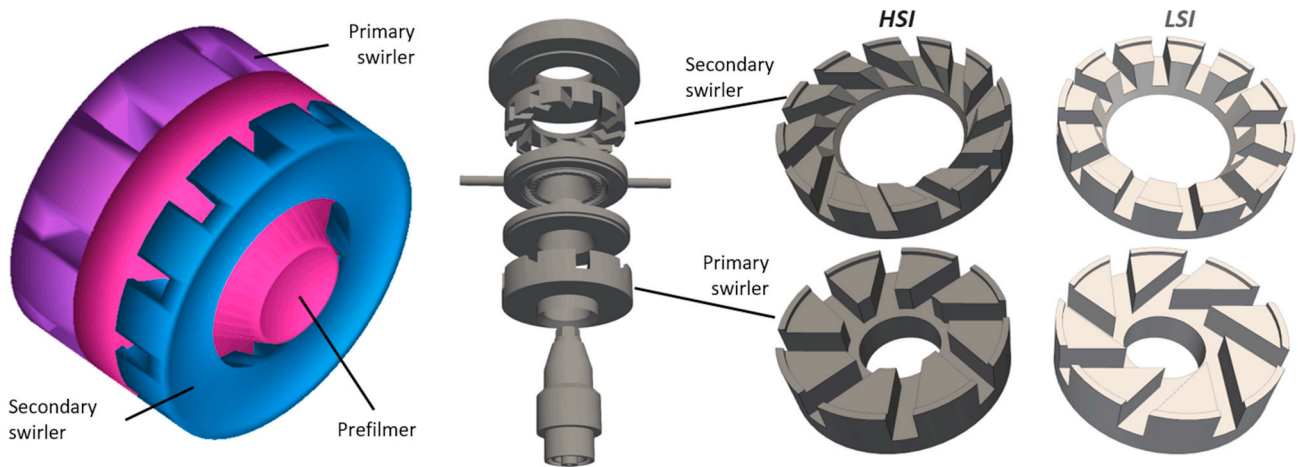

Fig. 3. Assembly and geometries of the primary and secondary swirlers.

comparison to conventional nozzles operated with liquid fuels in aero-engines or stationary gas turbines, the main difference of the proposed construction is given by the preheating system for liquifying solid sulfur via the thermal oil cycle. There, the thermal conditioning for the sulfur supply has to be kept at a constant high temperature with over 400 K during the burner operation. Moreover, as sulfur has rather different material properties (e.g. density, viscosity, surface tension) compared with common hydrocarbon fuels, special attention has to be paid on designing the pipe system for molten sulfur.

3. Mathematical description

3.1. Governing equations

As a full resolution of the multiphase flow, starting from the primary breakup of the intact jet core to the secondary breakup of liquid ligaments into small-scale droplets, is computationally too expensive, a hybrid Euler-Lagrangian approach is used in the present work for modeling the multiphase interactions. In this case, a number of Lagrangian parcels are injected from given locations close to the atomizer, which are then tracked during the simulation [25–30]. These

parcels generally represent collections of spherical liquid droplets with similar characteristics, e.g. diameters and velocities. For the continuous Eulerian phase consisting of the gaseous mixture, the Favre-filtered conservation equations for mass, momentum, species masses and energy are solved in terms of LES

$$\partial_t \overline{\rho} + \nabla \cdot (\overline{\rho} \tilde{u}) = \overline{S}_\rho \tag{1}$$

$$\partial_t (\overline{\rho} \tilde{u}) + \nabla \cdot (\overline{\rho} \tilde{u} \tilde{u}) = -\nabla \overline{p} + \nabla \cdot (\overline{\tau} + \overline{\tau}^{sgs}) + \overline{\rho} g + \overline{S}_u \tag{2}$$

$$\partial_t \left(\overline{\rho} \tilde{Y}_k \right) + \nabla \cdot \left(\overline{\rho} \tilde{u} \tilde{Y}_k \right) = -\nabla \cdot \left(\overline{j}_k + \overline{j}_k^{sgs} \right) + \overline{r}_k + \overline{S}_{Y,k} \tag{3}$$

$$\partial_t \left(\overline{\rho} \tilde{H} \right) + \nabla \cdot \left(\overline{\rho} \tilde{u} \tilde{H} \right) - \partial_t \overline{p} = -\nabla \cdot \left(\overline{j}_q + \overline{j}_q^{sgs} \right) + \overline{q} + \overline{\rho} \tilde{u} g + \overline{S}_H \tag{4}$$

In Eqs. (1)–(4), $\overline{\cdot}$ denotes spatially filtered and $\tilde{\cdot}$ Favre-filtered values. ρ is the gas density, $\tilde{u}$ the velocity vector, $\overline{p}$ the pressure, g the gravitational acceleration and $\tilde{Y}_k$ the mass fraction of the k-th species. $\tilde{H} = \tilde{h}_s + \tilde{K}$ is the specific total enthalpy, with the specific sensible enthalpy $\tilde{h}_s$ and the specific kinetic energy $\tilde{K}$. $\overline{\tau}$ is the shear stress tensor due to non-uniform flow, $\overline{j}_k$ the diffusive mass flux of the k-th species due to

molecular diffusion and $\bar{\mathbf{j}}_q$ the heat flux due to thermal conduction. $\bar{r}_k$ and $\bar{q}$ are the reaction rate of the k-th species and the heat release rate caused by chemical reactions. $\overline{\boldsymbol{\tau}}^{sgs} = \overline{\rho}(\tilde{\mathbf{u}}\tilde{\mathbf{u}} - \widetilde{\mathbf{u}\mathbf{u}})$ and $\bar{\mathbf{j}}_{k|q}^{sgs} = \overline{\rho}(\tilde{\mathbf{u}}\tilde{\varphi} - \widetilde{\mathbf{u}\varphi})|_{\varphi=Y_k|H}$ are the subgrid scale stress tensor and scalar fluxes.

A corresponding set of equations for the conservation of mass, momentum and energy is solved for dispersed phase with the Lagrangian parcels:

$$\frac{dm_p}{dt} = \dot{m}_p \tag{5}$$

$$m_p \frac{du_p}{dt} = F_D + F_G \tag{6}$$

$$m_p c_{p,p} \frac{dT_p}{dt} = \dot{q}_c + \frac{dm_p}{dt} h_{ev} \tag{7}$$

with the mass, moving velocity and temperature of the parcel m_p, $\mathbf{u}_p$ and T_p. $\mathbf{F}_D$ and $\mathbf{F}_G$ are forces acting on the parcels according to aerodynamic drag and gravity. $\dot{m}_p$ indicates rate of evaporation of liquid droplets. The 1st term $\dot{q}_c$ on the r.h.s. of Eq. (7) denotes the convective heat transfer caused by the surrounding gas flow and the 2nd term on the r.h.s. of Eq. (7) represents the heat source due to evaporation, with the evaporation enthalpy h_{ev}. $c_{p,p}$ is the heat capacity of the dispersed phase. The discrete Lagrangian parcels are temporally advanced to their new positions according to the equation of motion at each simulation time step $d\mathbf{x}_p / dt = \mathbf{u}_p$, where $\mathbf{x}_p$ is the position vector.

3.2. Source term formulations

Coupling of the Eulerian phase with the gaseous mixture and the Lagrangian phase with the liquid droplets is considered by the source terms in Eqs. (1)–(7), which describe the transfer of mass, momentum, and heat between the Eulerian and Lagrangian phases. The Lagrangian conservation of mass is integrated into the Eulerian frame by the source term S_ρ, which is given by the evaporated mass of droplets in the cell volume per time step

$$S_\rho = \sum_{n=1}^{N_p} \left(\frac{\Delta m_p}{\Delta t} \right)_n \frac{1}{V_{cell}} \tag{8}$$

with Δm_p being the mass of evaporated liquid parcels, Δt the time step used for the carrier gas phase and V_{cell} the cell volume. Δm_p is deduced from time integration of the evaporation rate of droplet over V_{cell}. The calculation of the evaporation rate is further described in Sec.3.3.

The source term $\mathscr{S}_U$ considering the momentum exchange of the Eulerian phase with the parcels is calculated by

$$S_U = \sum_{n=1}^{N_p} \left(\frac{m_p(u_p - u_c)}{\tau_p} + \frac{\Delta m_p u_p}{\Delta t} \right)_n \frac{1}{V_{cell}} \\ \tau_p = \frac{4}{3} \frac{\rho_p d_p^2}{\mu_c C_D} \tag{9}$$

u_p and u_c represent the velocities of the parcels and the gas flow. m_p and Δm_p are the mass and the evaporated mass of liquid parcels. τ_p is the relaxation time of the particle, which characterizes the time required for a particle to adjust its velocity to the continuous phase velocity, reaching an equilibrium state. ρ_p and d_p are the density and diameter of the liquid parcels; μ_c is the dynamics viscosity of the gas phase and C_D the drag coefficient.

The source term $\mathscr{S}_{Yi}$ in the species mass equation (3) is analogous to Eq. (8), which is due to evaporation of the dispersed droplets

$$S_{Y,k} = \sum_{n=1}^{N_p} \left(\frac{\Delta m_{p,k}}{\Delta t} \right)_n \frac{1}{V_{cell}} \tag{10}$$

with the mass of the k-th species of the droplets $m_{p,k}$.

The energy source term with respect to heat transfer between the gas and liquid phase is calculated with

$$S_H = \sum_{n=1}^{N_p} \left(hA_p(T_p - T_c) - \frac{\Delta m_p h_{ev}}{\Delta t} \right)_n \frac{1}{V_{cell}} \tag{11}$$

where h is the convective heat transfer coefficient (see Sec.3.3) and h_{ev} the enthalpy of evaporation. A_p is surface area of the droplet. T_p and T_c are the temperature of droplet and continuous gas flow.

The main force acting on a droplet is given by the drag force $\mathbf{F}_D$ caused by surrounding gas flow

$$F_D = m_p \frac{u_c - u_p}{\tau_p} \tag{12}$$

By assuming sperhical droplet, the drag coefficient C_D in τ_p in Eq. (9) and Eq. (12) is determined in terms of the droplet's Reynolds number Re [31].

$$C_D = \frac{24}{Re}\left(1 + 0.15Re^{0.687}\right) \text{ for } Re \leq 1000 \\ C_D = 0.44 \text{ for } Re > 1000 \tag{13}$$

3.3. Phase change and heat transfer model

The evaporation rate in Eq. (5) is evaluated following the Spalding correlation [32].

$$\dot{m}_p = -\pi d_p \, Sh \, \rho_c D_F \ln\left(1 + \frac{Y_{F,\zeta} - Y_{F,\infty}}{1 - Y_{F,\zeta}}\right) \tag{14}$$

where $Y_{F,\zeta}$ and $Y_{F,\infty}$ are the mass fractions of evaporated fuel in the film surrounding the droplet surface and at the far field respectively. ρ_c is the density of the carrier gas and D_F the diffusivity. The Sherwood number Sh is calculated by the Ranz-Marshall correlation [33].

$$Sh = 2 + 0.6Re^{1/2}Sc^{1/3}, \ 0 \leq Re < 200, \ 0 \leq Sc < 250 \tag{15}$$

where Sc is the Schmidt number and ν_p the kinematic viscosity.

Analogously, the convective heat transfer from the carrier gas to the particle in Eq. (7) is given by

$$\dot{q}_c = \pi d_p \lambda_F Nu \ (T_c - T_p) f_{heat}, f_{heat} = \frac{-\frac{c_{p,c}\dot{m}_p}{\pi d_p \lambda_F Nu}}{e^{-\frac{c_{p,c}\dot{m}_p}{\pi d_p \lambda_F Nu}} - 1} \tag{16}$$

with λ_F being the thermal conductivity. The Nusselt number Nu is evaluated according to the Ranz-Marshall correlations for heat transfer between a single sphere and its surrounding gas flow

$$Nu = 2 + 0.6Re^{1/2}Pr^{1/3}, \ 0 \leq Re < 200, 0 \leq Pr < 250 \tag{17}$$

with the Prandtl number Pr and the heat capacity $c_{p,c}$ of the carrier gas. D_F and λ_F are evaluated based on species concentrations and temperature in the film surrounding the droplet surface, which are evaluated as weighted average with 1/3 of the carrier gas and 2/3 of droplet properties ("1/3 rule"). The carrier gas properties, such as viscosity or heat capacity, have been determined by means of the temperature and the mixture composition considering all participating chemical species.

3.4. Turbulence and combustion modeling

The turbulent flow field has been modeled with the large eddy simulation (LES) technique [34], which solves the Favre-filtered set of governing equations (1)–(4) in the Eulerian phase and models the influence of unresolved turbulent fluctuations by means of a subgrid scale (SGS) model. LES is able to resolve turbulent flow structures till the cut-off scale. Therefore, it is well suited for studying flow and combustion dynamics in cases, where the flow field of concern is highly

unsteady and dominated by large-scale turbulent motions [35]. In the current work, the algebraic Smagorinsky model has been used for modeling the SGS viscosity or Reynolds stresses [34]. Unresolved scalar fluxes have been considered by a gradient transport approach using a constant turbulent Schmidt/Prandtl number of unity.

The partially stirred reactor (PaSR) model [36,37] is used for evaluating the chemical reaction rates, along with a detailed reaction mechanism for the oxidation of sulfur [38]. For considering the flame-turbulence interaction in the Eulerian phase, the PaSR concept regards one part of the cell as reacted and the other part as non-reacted. The reacted part is calculated as a perfectly stirred reactor using a finite rate chemistry formulation. Species are then mixed with a certain mixing time according to local turbulence condition. In this way, a weighted reaction rate due to turbulence-chemistry interaction can be formulated, employing a chemical and a SGS turbulent time scale τ_{chem} and τ_{mix}

$$\bar{\dot{r}}_k = \frac{\tau_{chem}}{\tau_{chem} + \tau_{mix}} \dot{r}_k \tag{18}$$

The effect of unresolved SGS scalar transport on the reaction rate calculation is considered by the competition between the chemical and the SGS turbulent time scales. For $\tau_{chem} \ll \tau_{mix}$ with a large Dahmköhler number $Da = \frac{\tau_{mix}}{\tau_{chem}} \gg 1$ (corresponding to large grid cells), the mean reaction rate is limited by the turbulent mixing time due to $\bar{\dot{r}}_k \propto \frac{1}{\tau_{mix}}$. For $\tau_{chem} \gg \tau_{mix}$ or $Da \ll 1$ (corresponding to small grid cells), the reaction rate approaches asymptotically the laminar reaction rate $\dot{r}_k$, indicating a weak influence of turbulent flow on the mean reaction rate. One drawback of the method may be given by the linear weighting of reaction rate by means of τ_{chem} and τ_{mix}, which is valid only for the limits with $Da \gg 1$ or $Da \ll 1$. In addition, the evaluation of τ_{mix} from the SGS modeling may have an impact on the calculation of the filtered reaction rate.

In the current work, liquid sulfur is injected into hot air at a temperature higher than the auto-ignition temperature of sulfur (see Sec.4), so that the mechanism for flame stabilization in this case is assumed to be determined by auto-ignition, instead of flame propagation. This behaviour has been confirmed by calculations of 1D unstrained premixed flames with detailed transport and reaction models, where flame stabilization cannot establish at the given pre-heated condition for a wide range of equivalence ratios. Therefore, the state-of-the-art modeling concepts [11–16,19,39], e.g. the artificially thickened flame (ATF), Flamelet/progress variable (FPV) or the probability density function (PDF) concepts using steady-state, laminar flame structures for chemistry tabulations, are not suited here to describe transient effects such as auto-ignition. By using the chemical kinetic law for evaluating the reaction rates, spontaneous variation in the mixture composition or temperature, possibly due to the evaporation process, is directly adopted, which may, however, represent a limitation for other reaction models due to inhomogeneous or mixed-mode combustion. One major drawback of the PaSR model is given by calculations of the species reaction rates with detailed reaction kinetics, which is computationally expensive for reaction mechanisms with a large number of chemical species and elementary reactions.

3.5. Other submodels

The secondary breakup of droplets has been considered by using Reitz Diwaka's breakup model [40], where initial droplets can further break down into smaller droplets based on the local droplet Weber number *We*. As droplet collisions play an important role in case of dense sprays [41,42], the deterministic-stochastic model proposed by O'Rourke [31,43] is used to account for collisions between individual droplets. The model calculates the probability of collision for each pair of parcels in each cell volume and determines the type of interaction, i. e., coalescence or grazing, based on the collisional Weber number and the relative radii of the colliding droplet pair. The states of the two

colliding parcels are then modified based on the outcome of the collision. The rebound model from the droplet impingement regimes for dry wall [44] has been applied for the droplet-wall interaction, assuming that the wall temperature is above the boiling temperature of the liquid and the droplet Weber number is small ($We \ll 1$). In this case, droplets impinging against the wall are bounced back without energy loss. As the combustion products of sulfur with SO_2 or SO_3 are quite corrosive, more sophisticated models accouting for the droplet-wall interaction and heterogeneous wall reactions may become an important issue. The effect of the SGS velocity on droplet motion has been neglected, assuming a large droplet relaxation time compared with the SGS time scale.

Main objective of the present work is to address the variation of flame stabilization behaviour while modulating the swirl number of the nozzle, for instance, in order to avoid the contact of sulfur droplets with the wall. For this reason, only common physical sub-models have been applied, which are already implemented in the OpenFOAM code. An extensive description as well as validation of these models are out of scope of the present work. Nonetheless, similar modeling strategies regarding spray and/or combustion modeling have been used in previous works [28,37,45–47], where the simulation results showed reasonably good agreement with corresponding experiments.

4. Numerical setups

As the internal flows generated by the swirlers within the nozzle have a significant impact on the resulting spray and combustion characteristics downstream, the computational domain is deliberately built to cover a major part of the nozzle. As depicted in Fig. 4, the geometry includes the pressure atomizer located along the centreline axis, two annular oriented radial swirl generators, the prefilmer and the diffusor (see also Figs. 2 and 3). The combustion chamber with a cylindrical shape has the dimensions of length $\times$ diameter = 200 mm $\times$ 160 mm. Preheated air enters the domain from the annular boundary on the left, which is redirected to pass through the primary and secondary swirlers. The combustion chamber is treated as adiabatic, no-slip wall. Normal to the outlet boundary, gradients of all transport variables are set to zero and the total pressure is set to 1 bar. The computational grid consists of approx. 15 million tetrahedral elements, using an equidistant resolution (cubic root of cell volume) of 0.33 mm inside the nozzle and 0.67 mm in the combustion chamber.

The mass flow rates of sulfur and air are $\dot{m}_{sulfur} = 6.1$ kg/h and $\dot{m}_{air} = 37.5$ kg/h, leading to a thermal load of $\dot{Q} = 19.1$ kW and an equivalence ratio of $\Phi = 0.7$ (fuel-lean). Solid sulfur is liquified by heating it up to $T_{sulfur} = 413$ K, which is then led into the pressure atomizer. The airflow is preheated to $T_{air} = 720$ K, which corresponds to a temperature of compressed air from ambient condition to 15 bar, considering an isentropic efficiency of 85% of the compressor. The Reynolds number based on the bulk flow velocity of air $U_0 = 25.3$ m/s and the nozzle diameter at the exit plane $D_0 = 32.7$ mm is $Re = 12,000$. A summary of the operating conditions used in this work is shown in Table 1, which remain the same for both HSI and LSI nozzle configurations (see Fig. 3).

The simulations have been performed with the open-source code OpenFOAM [48], which solves the governing equations by means of the finite volume method. The simulations employ a fully compressible formulation of the governing equations, along with an implicit scheme (Euler) for the time integration and the central difference scheme (second order, unbounded) for the spatial discretization of the convective and diffusive terms. The pressure-implicit split-operator (PISO) algorithm has been used for pressure correction [49]. As the OpenFOAM code provides material properties only for a limited number of liquid fuels, the required material properties of sulfur, such as the density, the viscosity or the heat capacity for both liquid and gaseous phases, have been implemented into OpenFOAM as functions of state variables according to the data sheet provided by NIST [50]. Table 2 lists some of the most important physical parameters of liquid sulfur under the conditions
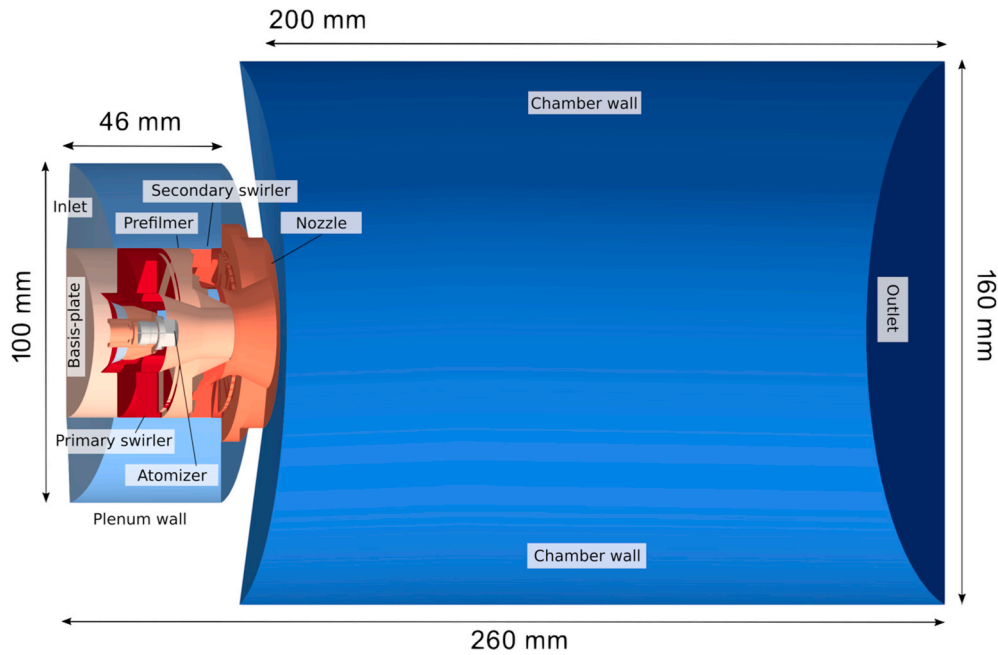
Fig. 4. Computational domain and boundary conditions.

Table 1
Operating conditions for sulfur combustion.

p [bar]	T_{air} [K]	T_{sulfur} [K]	$\dot{m}_{air}$ [kg/h]	$\dot{m}_{sulfur}$ [kg/h]	Re [−]	Φ [−]	$\dot{Q}$ [kW]
1	720	413	37.5	6.1	12,000	0.7	19.1

Table 2
Important physical properties of liquid sulfur at 1 atm and 413 K.

ρ [kg/m³]	T_{melt} [°C]	T_{boil} [°C]	T_{ign} [°C]	μ [mPas]	σ [mN/m]	h_{ev} [kJ/mol]	Hu_{sulfur} [MJ/kg]
1819	115.2	444.6	232	7.8	59	45	11.3

given in Table 1, with the density ρ, the melting temperature T_{melt}, the boiling temperature T_{boil}, the auto-ignition temperature T_{ign}, the dynamic viscosity μ, the surface tension σ, the heat of evaporation h_{ev} and the heating value Hu_{sulfur}. In addition, a detailed reaction mechanism including the species S, S_2, SO, SO_2, SO_3, O_2, O, N_2 has been used for calculating the sulfur/air combustion reactions [38]. The parameters of injected Lagrangian sulfur droplets, such as injection locations or size distributions, are described in Sec.5.2.
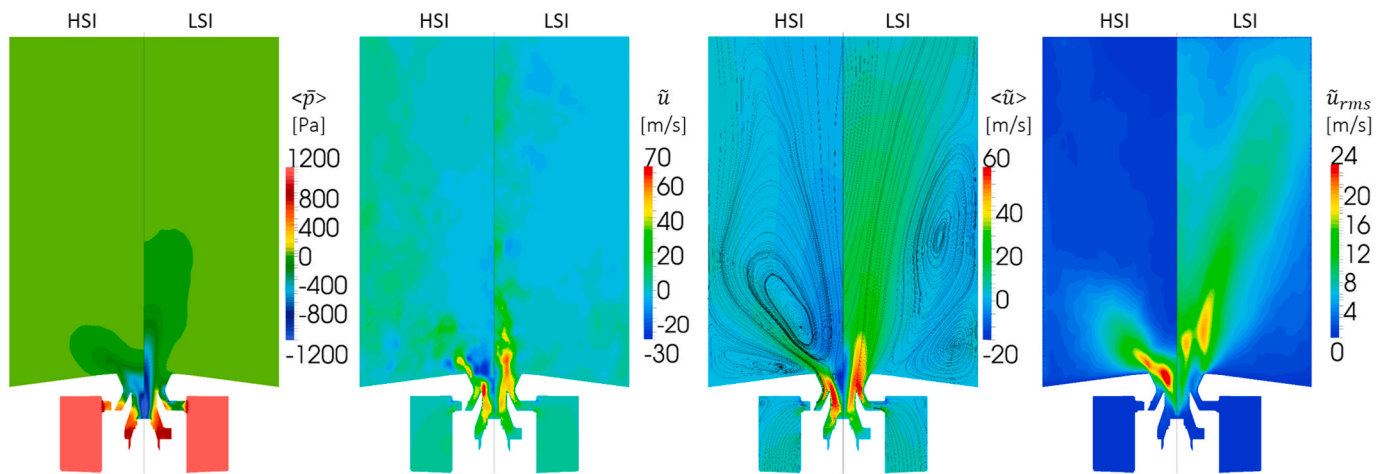

Fig. 5. Comparison of contours of a) time mean pressure, b) instantaneous streamwise velocity, c) time mean streamwise velocity and d) time root mean square (rms) streamwise velocity, on a cutting plane passing through the centerline axis for the HSI (left part) and LSI (right part) nozzle configurations.

5. Results and discussions

5.1. Non-reactive flow

The turbulent flow field generated by the interior nozzle design is of significant importance for the spray dispersion and evaporation, which further influence the mixing process and flame stabilization. Thus, the simulations have first been conducted for solely the gaseous flow without liquid sulfur, in order to study the dominant flow patterns generated by the double-concentric swirl nozzles. Coarse grids with 8 million cells and an overall equidistant resolution of 0.8 mm are used in this case. Fig. 5 from left to right shows contours of calculated a) time averaged $\bar{p}$, b) instantaneous streamwise resolved velocity, c) time averaged $\tilde{u}$ and d) time root mean square (rms) values of streamwise velocity, for a cutting plane passing through the centerline axis; the left and right parts of each single plot represent results for the HSI and LSI configurations. The mean pressure shown in Fig. 5a yields a large gradient in the transverse direction inside the nozzle, which results in centrifugal forces acting on the fluid to sustain the swirled flow motion. The lowest pressure is found at the location, where the airflow from the primary swirler enters the prefilmer. As the gas flow reaches the outlet plane of the nozzle, the tangential movement diminishes strongly due to expansion of the flow domain, so that the centrifugal force required for the rotational movement decreases, leading to an adverse pressure gradient along the streamwise direction. As a consequence, a backflow region with negative streamwise velocity along the axis is generated in this case (recirculation zone), as shown in Fig. 5b by contours of the streamwise flow velocity.

In Figs. 5c and 2D time-mean streamlines are used to visualize dominant flow structures. The calculated flow field for the burner configuration with a higher SI exhibits a large inner recirculation zone (IRZ) and a small outer recirculation region at the corner of the chamber. The IRZ is characterized by a large backflow region with negative streamwise velocities, which leads to strong spreading of the main flow. As mentioned before, the IRZ is generated by the adverse pressure

gradient, where the static pressure increases along the streamwise direction (see Fig. 5a). On the contrary, the LSI configuration with a small swirl intensity is dominated by an outwardly recirculating vortex (see the right half of Fig. 5c), which advances the main jet flow towards the centerline. For the LSI case, a small IRZ can be detected in Fig. 5b by the negative flow velocity near the nozzle exit. This is again due to the adverse pressure gradient caused by the swirled flow motion, which leads to a slight spreading of the main jet. However, the pressure gradient is weaker in the LSI case compared with the HSI case, as shown in Fig. 5c. The simulation results reproduce expected behaviours regarding characteristic flow patterns caused by the swirled flows, as already manifested in previous experimental and numerical works using similar nozzle designs [20,22,51]. The time rms value of the flow velocity shown in Fig. 5d represents a measure of local turbulence intensities, which controls the operational performance of underlying physical processes such as liquid atomization, spray evaporation, gas phase mixing and combustion. The highest turbulent fluctuations are found to be closely located to the nozzle exit for the HSI case, whereas large rms flow velocities are detected further downstream in the combustion chamber for the LSI nozzle. As the overall reaction rates are strongly correlated with the turbulent fluctuations due to the effect of flame-turbulence interaction, the flame stabilizes mostly at the locations with the largest turbulence intensities (see Fig. 8 on the right with snapshot of local heat release rate).

5.2. Spray dispersion

In a second step, discrete Lagrangian parcels rendering the sulfur droplets are injected from an annular disk (inlet for liquid sulfur) into the computational domain, which reproduces a hollow cone spray downstream. The orifice of the prefilmer is located 11 mm upstream of the exit plane of the nozzle, with an inner and an outer diameter of 15 mm and 16 mm (see Fig. 2). The injection area of liquid sulfur is closely aligned with the orifice of the prefilmer, laying 2 mm downstream of the prefilmer with an inner and an outer diameter of 12 mm and 17 mm
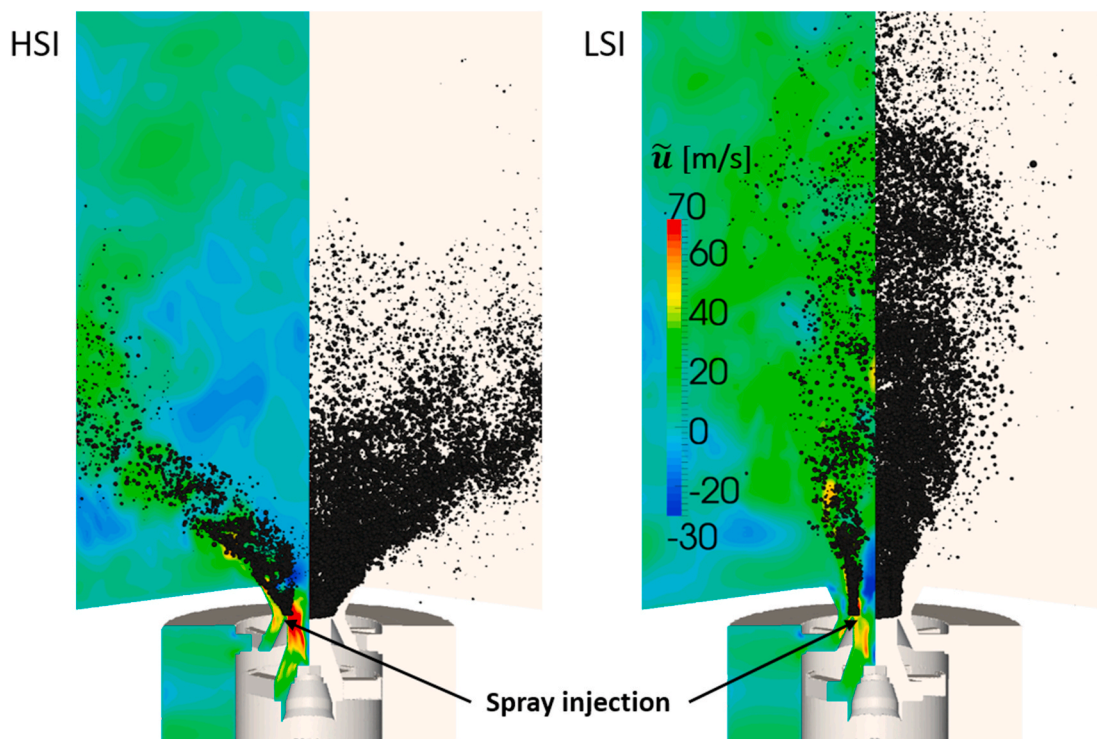

Fig. 6. Comparison of spray distributions caused by the HSI (left) and LSI (right) nozzles: the droplets are illustrated on the left half for a cutting plane through the centerline axis and on the right half with a full 3D representation.

(indicated in Fig. 6). The Rosin-Rammler distribution [52] is used for the initial size distribution of the droplets at the given injection locations, having a Sauter-Mean-Diameter (SMD) of 50 m. The injection area and size distributions are adjusted according to corresponding PDA (Phase Doppler Anemometry) measurement of the sulfur spray generated by the nozzle under atmospheric, non-reactive conditions. There, the calculated radial distributions of liquid mass with the given injection parameters compare well with the measured data. In fact, neglecting the primary atomization in spray simulation and injecting droplets at a specified fictional area represent state-of-the-art technology for modeling spray combustion in order to reduce computational cost. Although the assumptions used by such injection models differ from the real primary breakup physics, the method has enabled simulations of spray combustion processes in realistic geometries and provides reasonaly good results [26,51].

The injected molten sulfur has a temperature of 413 K, which is lower than the ambient preheated air temperature at 720 K (see Table 1). Therefore, sulfur droplets are heated up by the hot airflow, until they evaporate and mix with air to an ignitable mixture. Preliminary chemical kinetic calculations in a 0D homogeneous reactor predict that the ignition delay time of sulfur/air mixtures at 720 K and 1 bar is of the order of 1 ms (see Fig. 10 too), which is as large as the residence time of the sulfur droplets traveling from the injection locations to the reaction zone. In addition, the auto-ignition temperature of sulfur is lower than the hot air temperature (see Table 2). Hence, the fuel-air mixture auto-ignites in the simulations, without using additional heating or ignition sources.

Fig. 6 compares the spray dispersions caused by both HSI and LSI nozzle configurations, where the left part of each sub-plot shows contours of the instantaneous streamwise velocity, along with a 2D view of droplet distributions on a meridian cutting-plane, and the right part of Fig. 6 presents a 3D view of the droplet distribution. The particle sizes are scaled by a factor of 50 for visualization. The droplets shown in Fig. 6 represent the portion of liquid in an initial stage shortly after the injection, whereas most of the liquid fuel mass introduced before is already evaporated and burnt by mixing with ambient hot gas. For the HSI case, the IRZ forces sulfur droplets to recirculate back to the nozzle, which causes a large spreading angle of the spray and leads to many sulfur droplets hitting the chamber wall. In addition, the IRZ leads to a large residence time for the droplets, which is favorable in terms of multiphase heat and mass transfer. The droplets are therefore

completely evaporated already in the lower half of the combustion chamber and no unburnt sulfur droplets can be detected at the outlet plane. For the LSI configuration, the sulfur droplets yield a smaller spray angle compared with the HSI case due to the low swirl intensity of airflow. A small number of droplets reach the outlet plane of the combustion chamber, which is attributed to the high streamwise momentum or velocity of the airflow. However, only few droplets hit the chamber wall in the LSI compared with the HSI configuration.

Fig. 7 depicts 3-dimensional side views of sulfur droplets by using the HSI and LSI nozzle configurations, which are colored by their streamwise velocities on the left and temperatures on the right. As discussed before, the IRZ caused by the highly swirled flow leads to a strong dispersion of the spray with a large residence time for the convective heat and mass transfer between different phases. Consequently, the streamwise velocities of droplets are smaller and the temperatures of droplets are higher for the HSI compared with the LSI burner. In this case, the HSI burner yields a faster evaporation of sulfur droplets compared with the LSI case, revealing a complete evaporation of injected liquid fuel. In contrast, a small amount of liquid fuel leaves the computational domain in the LSI case, leading to an overall evaporation rate of approx. 99% (ratio of evaporated to introduced mass of sulfur).

5.3. Flame stabilization

After evaporation of the droplets, the sulfur vapour mixes further with ambient air and combustion reactions take place, accompanied by strong heat release. Fig. 8 illustrates contours of the gas phase temperature $\tilde{T}$ on the left and the resolved heat release rate $\overline{\overline{q}}$ on the right, where $\overline{\overline{q}}$ is calculated by means of summing up the products of the reaction rates and the formation enthalpy of all chemical species. The left half of each plot in Fig. 8 denotes the instantaneous and the right half the time averaged fields. The reaction zone can be identified either by the large gradient of temperature or the regions with a large heat release rate. The reaction zone is corrugated by the turbulent flow due to flame-turbulence interaction. The HSI nozzle causes strong recirculation of hot product gas to the flame root by the IRZ (see Fig. 5c), which leads to a V-shaped flame anchored to the nozzle, leading to an enhanced flame stabilization. In contrast, the fuel droplets move faster in streamwise direction for the LSI case due to the high longitudinal momentum of the airflow (see Figs. 5b and 7 on the right for the streamwise velocities of gas and droplets), which results in a larger penetration range of the
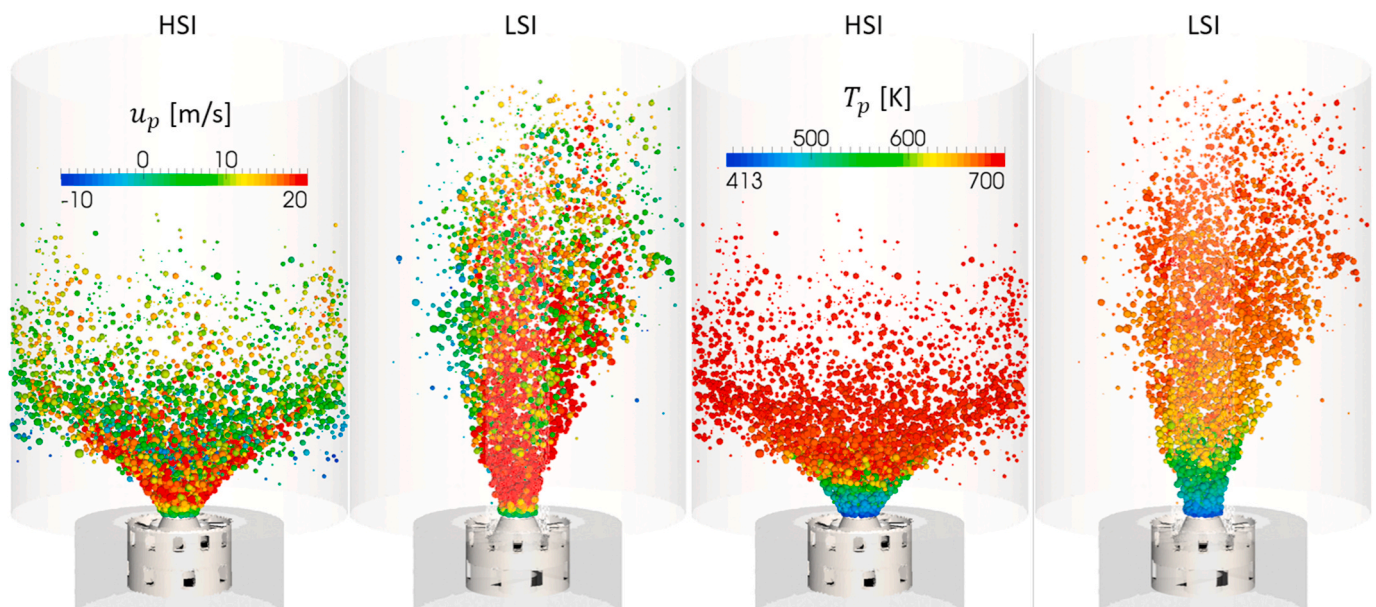

Fig. 7. Calculated droplet dispersions, streamwise velocities and temperatures by using the HSI and LSI nozzle designs.
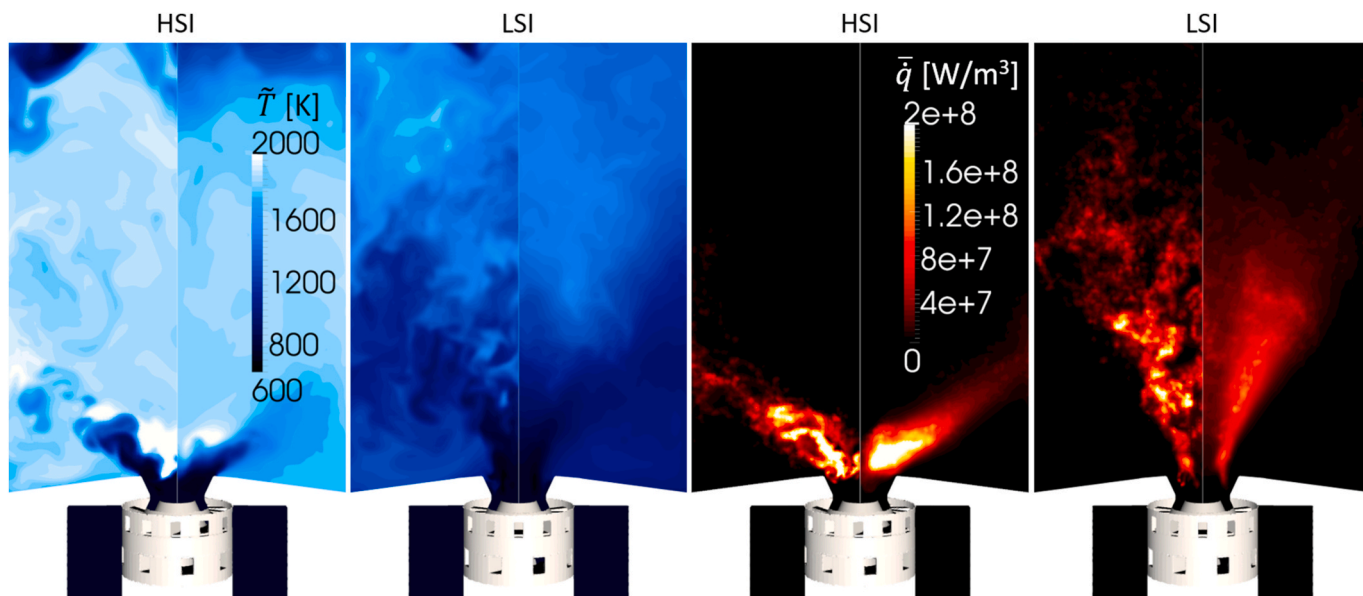
Fig. 8. Comparison of instantaneous (left half in each plot) and time averaged (right half in each plot) contours of resolved temperature (left) and heat release rate (right) by using the HSI and LSI burner designs.
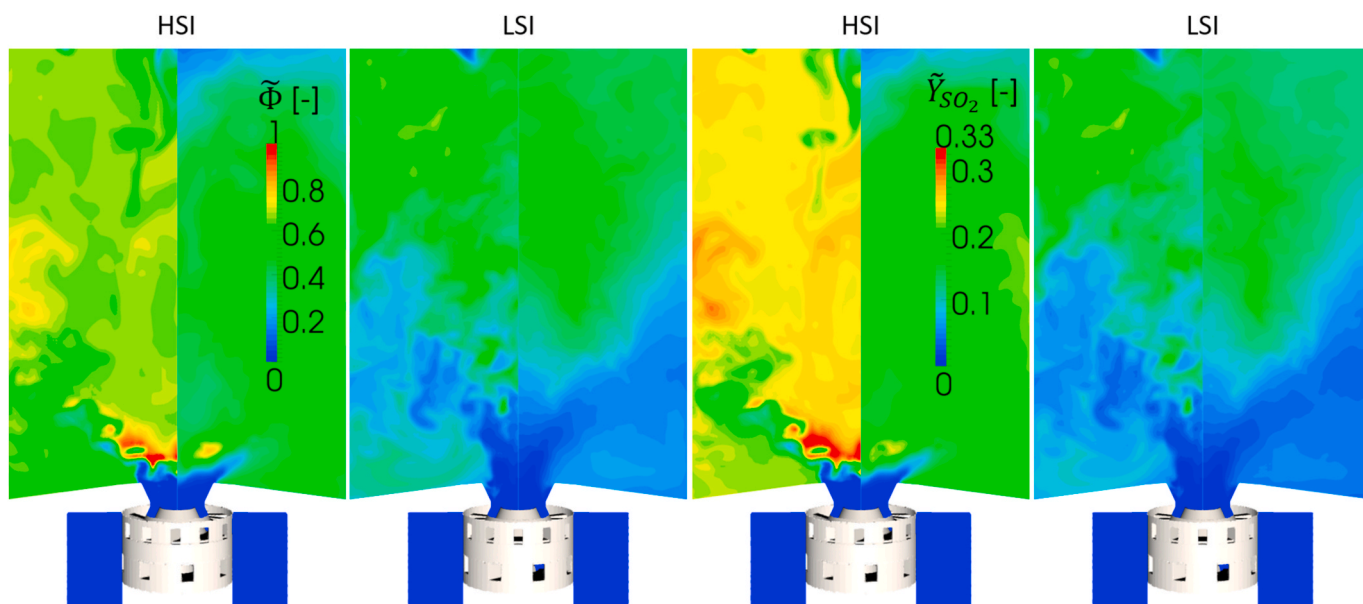

Fig. 9. Comparison of instantaneous (left half in each plot) and time averaged (right half in each plot) contours of local equivalence ratio (left) $\tilde{\Phi}$ and mass fraction of SO₂ $\tilde{Y}_{SO_2}$ (right) by using the HSI and LSI burner designs.

spray. Therefore, the reaction zones with large heat release rate extend further downstream for the LSI burner, before a complete consumption of the sulfur droplets is achieved.

The maximum flame temperature is approx. 2000 K for the HSI flame, whereas it is considerably lower in the LSI case (see Fig. 8 on the left). This is attributed to the fact that the HSI configuration yields locally a higher evaporation rate and an enhanced mixing of sulfur vapour with air caused by the strong recirculating flow. This behaviour is illustrated in Fig. 9 on the left by contours of the local fuel equivalence ratio Φ, which is evaluated by means of the ratio of available mass fraction of sulfur gathered from all chemical species to the stoichiometric mass fraction of sulfur in the gaseous phase (considering a global one-step reaction converting sulfur to sulfur dioxide). Although the global equivalence ratio according to the initial fuel and air mass flows is $\Phi = 0.7$ (see Table 1), Φ reaches locally stoichiometric conditions of

unity in the HSI case due to the intense evaporation and mixing caused by the IRZ. In addition, Φ is overall larger in the HSI compared with the LSI case, so that sulfur is burned under fuel-leaner conditions in the LSI case. The temperature distribution correlates strongly with the contours of Φ as well as the mass fraction of SO₂ (see Fig. 9 on the right). The results reveal that the HSI nozzle leads to a higher flame temperature and SO₂ concentration compared with the LSI nozzle, due to the stronger evaporation and mixing processes sustained by the IRZ or strongly swirled airflow, respectively. The opposite case is found for the SO₃ species due to combustion at fuel-leaner conditions (smaller Φ) for the LSI compared with the HSI case. The same trend has been confirmed for the concentrations of SO₂ and SO₃ integrated over the outlet area using their time averaged values by comparing the HSI and LSI nozzles.

The results are further supported by 0-dimensional calculations of homogeneous reactors with premixed sulfur/air mixtures at the
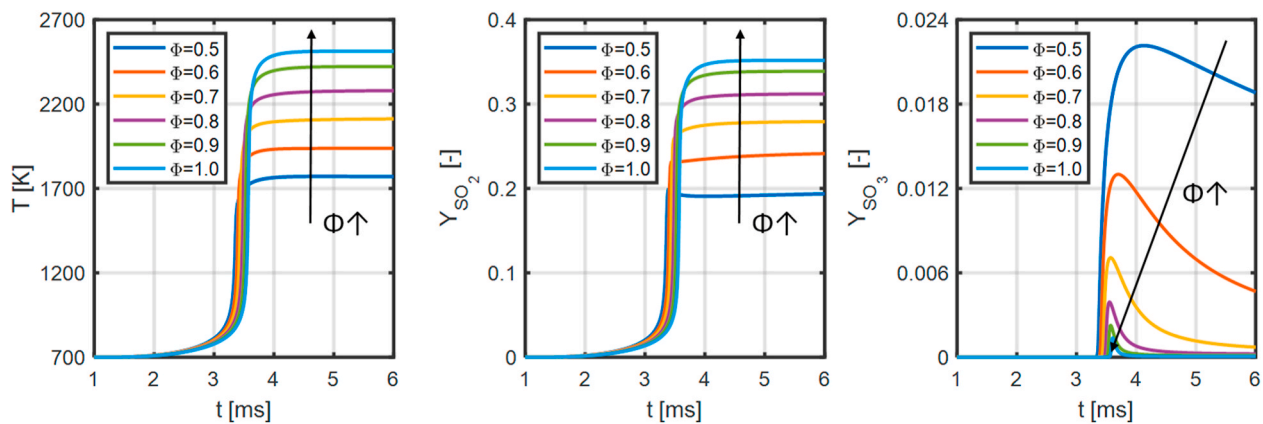
Fig. 10. Temporal evolution of temperature, mass fractions of SO_2 and SO_3 from calculations of auto-ignition of sulfur/air mixtures at different equivalence ratios in 0D homogeneous reactors at 1 bar and 700 K.

conditions of 1 bar and 700 K initial pressure and temperature, using the same reaction mechanism [38] as applied for the simulations of the sulfur burner. As shown in Fig. 10, the temperature (left) and mass fraction of SO_2 (middle) are strongly correlated with each other, increasing monotonously with the equivalence ratio Φ. On the contrary, the mass fraction of SO_3 (on the right of Fig. 10) is considerably lower at increased Φ. This explains the flame behaviours caused by the HSI and LSI burner configurations. The strongly recirculating flow in the HSI burner causes combustion occurring at a higher equivalence ratio compared with the LSI case, which leads to an overall higher flame temperature and SO_2 concentration. The ignition delay time can be identified from Fig. 10, which is almost constant at around 3.5 ms for all cases with different Φ. Due to the recirculating vortices, the ignition delay time is sufficiently small compared with the residence time measured by the chamber length and the mean streamwise velocity, ensuring a complete and stable burning of the sulfur spray.

Fig. 11 plots conditionally averaged heat release rate $\bar{q}|_\Phi$ with respect to Φ, which is evaluated for a time instant for the HSI and LSI nozzle. $\bar{q}|_\Phi$ is larger than zero even at $\Phi \approx 0$, which is also observed in 0D auto-ignition calculations and confirms again the auto-ignition behaviour of sulfur under the current operating condition. The range of Φ with the largest contribution to the overall heat release rate is detected close to $\Phi \approx 0.9$. Similar results have been reported in Refs. [53,54] by means of

2D direct numerical simulations of gas phase combustion and spray flame–vortex interaction, where ignition or bulk heat release was found to be attributed to a well-defined or preferred mixture fraction, identified as "most reactive" in Refs. [53]. As the HSI flame is characterized by a more intense mixing compared with the LSI nozzle due to the IRZ, the range of "most reactive" mixture composition is found at larger Φ values for the HSI compared with the LSI case. In addition, the maximum of $\bar{q}|_\Phi$ is larger for the HSI nozzle, which explains the higher overall temperature for the HSI case depicted in Fig. 8 on the left.

It should be noted that the results presented in this work are valid solely for the current burner configuration with sulfur as fuel. As the flame stabilization is achieved through auto-ignition, one uncertainty factor may be connected with the chemical reaction mechanism used in this work. As shown in Refs. [38,55], applying different reaction mechanisms for sulfur combustion has led to significant differences in the ignition delay time and the laminar flame speed. In addition, the most common structure of elemental sulfur in nature is the octasulfur S_8 (solid), whereas the diatomic molecule S_2 is used in this work for sulfur vapour. Although not shown here, simulation results using a twice-coarsened grids for the HSI and LSI nozzles showed qualitatively similar flame stabilization behaviour and overall flame structures as obtained in the present work. Hence, the main conclusion regarding comparison of varied nozzle configurations remains unchanged whilst using different grid resolutions.
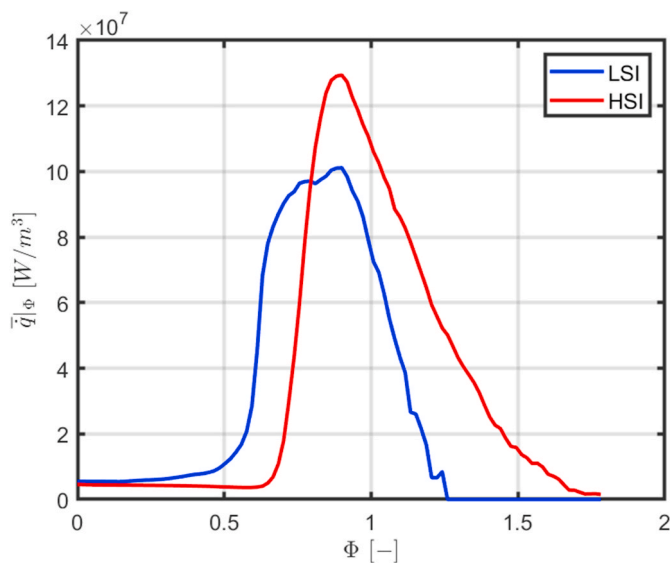
6. Conclusion

A novel double-concentric swirl burner is introduced in this work for the efficient and clean combustion of sulfur with a high power density ($\tilde{}$ 5 MW/m^3). The burner serves as a key component of a solar power cycle, which is able to store solar energy by means of elemental sulfur and generate electricity by burning sulfur via the proposed combustor system. In order to assess applicability of the preliminary design concepts, highly-resolved numerical simulations have been performed. The computational grids consist of approx. 15 million finite volumes and cover major components of the nozzle, such as the primary and secondary swirler. The underlying chemo-physical phenomena such as the turbulent flow, spray and chemical reactions have been considered in detail by using physical models. In this way, the simulations provide an insight into the main features of the complex flow patterns and flame stabilization, allowing an initial assessment of the burner design. The simulation results reproduce the expected characteristic behaviours regarding dominant flow patterns, spray dispersion, evaporation, mixing, ignition and flame stabilization, as already manifested in previous experimental works using similar nozzle designs but different fuels.

A detailed review has been conducted with respect to the influence of the swirl number of the airflow using two different arrangements of the

Fig. 11. Comparison of conditioanlly averaged $\bar{q}$ aginst local equivalence ratio for the HSI and LSI nozzles.

Table 3
Evaluation of different burner concepts based on results from numerical simulations.

	High Swirl Intensity (HSI)	**Low Swirl Intensity (LSI)**
Flow	Large inner recirculating ring vortices, small edge vortices, low streamwise velocity	Main inner jet flow, large outer recirculation vortices, high streamwise velocity
Spray	Large spray angle, low penetration range, fast evaporation, many droplets hitting the wall	Small spray angle, high penetration range, slow evaporation, few droplets hitting the wall
Flame	broad, short, high flame temperature	narrow, long, low flame temperature

primary and secondary swirlers. The nozzle with a high swirl intensity (HSI) provides a short, funnel-shaped flame attached to the burner, which is caused by a large inner recirculation flow (IRZ). Although the flame stability is improved by the IRZ, it leads to an overall high flame temperature at around 2000 K. In addition, a number of sulfur droplets hit the chamber wall, which makes the HSI design prone to damage on the combustion chamber and incomplete combustion. In contrast, the other nozzle with a low swirl intensity (LSI) yields an elongated jet flame distributed along the centerline axis, with few collisions of droplets with the chamber wall; an overall lower temperature at approx. 1500 K is observed for the LSI configuration compared with the HSI nozzle, which is favorable regarding NOx emissions. These main characteristics of applying different nozzle designs are summarized in Table 3. The achieved results suggest the further use of the LSI configuration due to the lower flame temperature and less droplet-wall collisions compared with the HSI case, which are beneficial in terms of long-term operability/lifetime and NOx formation of the burner system. The simulations provide a first insight into the complex phenomena of the multiphase, multi-scale reacting flows, which is useful in terms of computer-assisted design of novel burner systems, in particular for elaborate burner systems under extreme conditions. Further work includes simulations for varied equivalence ratio and elevated pressure conditions for the proposed burner design. In addition, more sophisticated modeling methods for the turbulence-flame interaction as well as the overall Lagrangian droplet tracking, e.g. for the droplet evaporation, will be used.

CRediT author statement

Feichi Zhang: Simulations of sulfur spray combustion, writing and editing. Hosein Heidarifatasmi/**Robert Wang**: generation of computational grids, implementation of material properties of sulfur. **Stefan Harth/ Michal Fedoryk:** Burner design. **Thorsten Zirwes/Nadia Sebbar:** Development of reaction mechanism, chemistry calculations. **Peter Habisreuther/Henning Bockhorn:** Supervision. **Dimosthenis Trimis**: Project administration, funding acquisition, supervision.

Declaration of competing interest

The authors declare that they have no known competing financial interests or personal relationships that could have appeared to influence the work reported in this paper.

Acknowledgments

References

[1] Renewable power generation by solar particle receiver driven sulphur storage cycle. https://www.pegasus-project.eu/.

[2] Wong B, Brown L, Buckingham R, Sweet W, Russ B, Gorensek M. Sulfur dioxide disproportionation for sulfur based thermochemical energy storage. Sol Energy 2015;118:134–44.

[3] Johnsson J, Glarborg P. Sulfur chemistry in combustion i: sulfur in fuels and combustion chemistry. In: Vovelle C, editor. Pollutants from combustion - formation mechanisms and impact on atmospheric chemistry. NATO ASI Series, Kluwer Academic Publisher; 2000. p. 263–82.

[4] Cheng-Kuan L, Lin R-T, Chen P-C, Wang P, De Marcellis-Warin N, Zigler C, Christiani DC. A global perspective on sulfur oxide controls in coal-fired power plants and cardiovascular disease. Sci Rep 2018;8(1):2611.

[5] Müller H. Ullmann's encyclopedia of industrial chemistry. 2000.

[6] Conroy E, Johnstone H. Combustion of sulfur in a venturi spray burner. Ind Eng Chem Res 1949;41(12):2741–8.

[7] King M, Moats M, Davenport W. Sulfuric acid manufacture: analysis, control and optimization. second ed. Amsterdam: Elsevier; 2013.

[8] Hogarth R, Jenkin C. A brief review of a portion of the literature dealing with sulphur burning and the formation and dissociation of sulphur trioxide. 2009.

[9] Sizikov V, Evseev V, Fateev A, Clausen S. Direct and inverse problems of infrared tomography. Appl. Optics 2016;55(1):208–20.

[10] Evseev V, Fateev A, Sizikov V, Clausen S, Nielsen KL. On the development of methods and equipment for 2d-tomography in combustion. In: Annual meeting of Danish physical society; 2011. p. 32.

[11] Sacomano Filho FL, Dreßler L, Hosseinzadeh A, Sadiki A, Krieger G. Investigations of evaporative cooling and turbulence flame interaction modeling in ethanol turbulent spray combustion using tabulated chemistry. Fluid 2019;4:187.

[12] Sacomano Filho FL, Kadavelil J, Staufer M, Sadiki A, Janicka J. Analysis of les-based combustion models applied to an acetone turbulent spray flame. Combust Sci Technol 2019;54–67.

[13] Franzelli B, Vié A, Boileau M, Fiorina B, Darabiha N. Large eddy simulation of swirled spray flame using detailed and tabulated chemical descriptions. Flow, Turbul Combust 2017;98:633–61.

[14] Sitte M, Mastorakos E. Large eddy simulation of a spray jet flame using doubly conditional moment closure. Combust Flame 2019;199:309–23.

[15] Sacomano Filho FL, Hosseinzadeh A, Sadiki A, Janicka J. On the interaction between turbulence and ethanol spray combustion using a dynamic wrinkling model coupled with tabulated chemistry. Combust Flame 2020;215:203–20.

[16] Hu Y, Kai R, Kurose R, Gutheil E, Olguin H. Large eddy simulation of a partially pre-vaporized ethanol reacting spray using the multiphase dtf/flamelet model. Int J Multiphas Flow 2020;125:103216.

[17] Eleonore R, Benedicte C, Poinsot T. Introducing chemical kinetics into large eddy simulation of turbulent reacting flows. Comput. Aided Chem. Eng. 2019;45:899–936.

[18] Sacomano Filho FL, Krieger G, van Oijen J, Sadiki A, Janicka J. A novel strategy to accurately represent the carrier gas properties of droplets evaporating in a combustion environment. Int J Heat Mass Tran 2019;137:1141–53.

[19] Galeazzo FCC, Fukumasu NK, Denev JA, Weis C, Habisreuther P, Filho GCK. Change in flame geometry of an ethanol spray flame by varying the spray characteristics. Combust Sci Technol 2019;191(9):1693–710.

[20] Kasabov P. Experimentelle Untersuchungen an abgehobenen Flammen unter Druck. Ph.D. Thesis. Universitätsverlag Karlsruhe Germany; 2014.

[21] Kasabov P, Habisreuther P, Zarzalis N. Experimental study on lifted flames operated with liquid kerosene at elevated pressure and stabilized by outer recirculation. Flow, Turbul Combust 2013;90(3):605–19.

[22] Merkle K. Einfluss gleich- und gegensinniger Drehrichtung der Verbrennungsluftströme auf die Stabilisierung turbulenter Doppeldrall-Diffusionsflammen. Ph.D. Thesis. Germany: Karlsruhe Institute of Technology; 2006.

[23] Merkle K, Hässler H, Büchner H, Zarzalis N. Effect of co- and counter-swirl on the isothermal flow- and mixture-field of an airblast atomizer nozzle. Int J Heat Fluid Flow 2003;24:529–37.

[24] Merkle K, Büchner H, Zarzalis, Sara ON. Influence of co and counter swirl on lean stability limits of an airblast nozzle. In: ASME turbo expo; 2003. GT2003–38004.

[25] Lebas R, Menard T, Beau P-A, Berlemont A, Demoulin F-X. Numerical simulation of primary break-up and atomization: Dns and modelling study. Int J Multiphas Flow 2009;35(3):247–60.

[26] Sanjose M, Senoner J, Jaegle F, Cuenot B, Moreau S, Poinsot T. Fuel injection model for euler–"euler and euler–"Lagrange large-eddy simulations of an evaporating spray inside an aeronautical combustor. Int J Multiphas Flow 2011;37(5):514–29.

[27] Gjesing R, Hattel J, Fritsching U. Coupled atomization and spray modelling in the spray forming process using openfoam. Eng. Appl. Comp. Fluid 2009;3(4):471–86.

[28] Zhou Z-F, Lu G-Y, Chen B. Numerical study on the spray and thermal characteristics of r404a flashing spray using openfoam. Int J Heat Mass Tran 2018;117:1312–21.

[29] Prosperetti A, Tryggvason G. Computational methods for multiphase flow. Cambridge university press; 2009.

[30] Yeoh GH, Tu J. Computational techniques for multiphase flows. Butterworth-Heinemann; 2019.

[31] O'Rourke P. Collective drop effects on vaporizing sprays. Ph.D. Thesis. United States: Princeton University; 1981.

[32] Spalding D. The combustion of liquid fuels. Williams and Wilkins; 1953.

[33] Ranz W, Marshall W. Evaporation from drops. Chem eng prog 1952;48(3):141–6.

[34] Fröhlich J. Large eddy simulation turbulenter Strömungen, vol. 1. Springer; 2006.

[35] Roux S, Lartigue G, Poinsot T, Meier U, Bérat C. Studies of mean and unsteady flow in a swirled combustor using experiments, acoustic analysis, and large eddy simulations. Combust Flame 2005;141(1–2):40–54.

[36] Kärrholm FP. Numerical modelling of diesel spray injection, turbulence interaction and combustion. Ph.D. Thesis. Sweden: Chalmers University of Technology Gothenburg; 2008.

[37] Novella R, García A, Pastor JM, Domenech V. The role of detailed chemical kinetics on cfd diesel spray ignition and combustion modelling. Math Comput Model 2011; 54(7–8):1706–19.

[38] Sebbar N, Zirwes T, Habisreuther P, Bozzelli J, Bockhorn H, Trimis D. S2+ air combustion: reaction kinetics, flame structure, and laminar flame behavior. Energ Fuel 2018;32(10):10184–93.

[39] Charles D, Moin P. Progress-variable approach for large-eddy simulation of non-premixed turbulent combustion. J Fluid Mech 2004;504:73–97.

[40] Reitz RD, Diwakar R. Effect of drop breakup on fuel sprays. SAE Trans 1986: 218–27.

[41] Sommerfeld M. Lagrangian modelling of droplet collisions in spraying systems. In: 8th European combustion meeting (ECM); 2017. Dubrovnik, Croatia.

[42] Sommerfeld M, Lain S. Numerical analysis of sprays with an advanced collision model. In: 28th conference on liquid atomization and spray systems. Valencia, Spain: ILASS); 2017. p. 418–31.

[43] O'Rourke PJ, Amsden A. A spray/wall interaction submodel for the kiva-3 wall film model. SAE Trans 2000:281–98.

[44] Lee S, SU R. Recent progress of spray-wall interaction research. J Mech Sci Technol 2006:1101–17.

[45] Yousefifard M, Ghadimi P, Mirsalim M. Numerical simulation of biodiesel spray under ultra-high injection pressure using openfoam. J Braz Soc Mech Sci 2015;37: 737–46.

[46] Peng Kärrholm F, Tao F, Nordin N. Three-dimensional simulation of diesel spray ignition and flame lift-off using openfoam and kiva-3v cfd codes. SAE Tech 2008: 2008-01-0961. https://doi.org/10.4271/2008-01-0961.

[47] Pichon T, Sabelnikov V, Moule Y, Cochet A. Assessment of a partially stirred reactor combustion model to predict the lean blow-out limit of a ramjet combustor. In: 18th AIAA/3AF international space planes and hypersonic systems and technologies conference; 2012.

[48] OpenFOAM. The open source cfd toolbox. https://www.openfoam.com/releases/openfoam-v1806/.

[49] Ferziger JH, Perić M. Computational methods for fluid dynamics, vol. 3. Springer; 2002.

[50] of Standards NI. Technology, Nist chemistry webbook. https://webbook.nist.gov/cgi/cbook.cgi?ID=C7704349 Mask=2 Type=JANAFL Plot=on.

[51] Keller J, Gebretsadik M, Habisreuther P, Turrini F, Zarzalis N, Trimis D. Numerical and experimental investigation on droplet dynamics and dispersion of a jet engine injector. Int J Multiphas Flow 2015;75:144–62.

[52] Lefebvre AH, McDonell VG. Atomization and sprays. CRC press; 2017.

[53] Mastorakos E, Baritaud T, Poinsot T. Numerical simulations of autoignition in turbulent mixing flows. Combust Flame 1997;109:198–223.

[54] Franzelli B, Vié A, Ihme M. Characterizing spray flame-vortex interaction: a spray spectral diagram for extinction. Combust Flame 2015;163.

[55] Zirwes T, Sebbar N, Habisreuther P, Harth S, Zhang F, Bockhorn H, Trimis D. Ignition behaviour of sulfur in air based on modified reaction kinetics. In: 11th mediterranean combustion symposium (MCS11). Spain: Tenerife; 2019.